# Mg dopants in lithium niobate ($LiNbO_3$, LN): Defect models and impact on domain inversion

A. Bocchini,[1,*] M. Rüsing,[1,2] L. Bollmers,[1,2] S. Lengeling,[1,2] P. Mues,[2] L. Padberg,[1,2] U. Gerstmann,[1] C. Silberhorn,[1,2] C. Eigner,[2] and W. G. Schmidt[1]

[1]*Department of Physics, Paderborn University, 33095 Paderborn, Germany*

[2]*Institute for Photonic Quantum Systems (PhoQS), Paderborn University, 33095 Paderborn, Germany*

(Received 7 March 2025; revised 20 May 2025; accepted 11 June 2025; published 8 July 2025)

The optical and ferroelectric properties of lithium niobate ($LiNbO_3$, LN), including the orientation of the ferroelectric domains, i.e., the poling behavior, are decisively influenced by dopants. In this study, we apply density functional theory (DFT) to understand the microscopic origin of the beneficial (and impairing) effects of different Mg-doping concentrations, including nominally undoped stoichiometric and congruent compositions, particularly on the ferroelectric domain inversion. $Mg_{Li}^{+}$ tends to be the dominant defect for lower doping concentrations, and a combination of $Mg_{Li}^{+}$ and $Mg_{Nb}^{3-}$ for intermediate doping concentrations. Single $Mg_{Li}$ defects are found to be a possible seed point for domain inversion, while the combination of $Mg_{Li}$ and $Mg_{Nb}$ defects is suggested to inhibit poling. In this case, the reaction pathways for the inversion are not symmetric and are characterized by different activation energies for each direction, which could promote the crystal to more easily revert to its original polarization.

DOI: 10.1103/5wz1-bjyr

## I. INTRODUCTION

The ferroelectric crystal lithium niobate ($LiNbO_3$, LN) features an advantageous combination of properties, which are used in many different applications, including optics, quantum communication, electronics, and piezotronics [1–7]. Most of the key material properties, like the piezoelectricity, second-order nonlinear response, or the electro-optic effect, are directly connected to the ferroelectricity and the orientation of the ferroelectric domains. Therefore, to harness any of these properties for applications, domain engineering and structuring are required. One example is the fabrication of periodically poled devices for nonlinear optics, which enable quasi-phase matching between the interacting beams [1]. Lithium niobate is available in various different qualities and stoichiometric compositions, such as stoichiometric LN, congruent LN, or MgO-doped LN. Stoichiometric LN refers to a composition that matches the chemical formula (Li:Nb ratio $\frac{[Li]}{[Nb]} = 1$). While stoichiometric LN can be synthesized with some effort [8,9], the most common and technologically most relevant composition corresponds to the so-called congruent LN. It results from a relatively simple fabrication of large-scale (up to 20 cm diameter), homogeneous single crystals via Czochralski growth [9]. Congruent LN is characterized by a Li:Nb ratio of $\frac{[Li]}{[Nb]} = 0.94$. The Li deficiency is a result of crystal growth at the congruent point, where the composition of the melt and solid crystal is identical. Here, crystallization can be controlled purely by temperature. In the phase diagram, this point is found at a Li:Nb ratio of $\frac{[Li]}{[Nb]} = 0.94$. To compensate for the lithium deficiency, so-called Nb antisite defects at Li sites ($Nb_{Li}$) form, where each is charge compensated by four Li vacancies [10–12].

The domain engineering in the congruent composition, however, is more challenging than for stoichiometric crystals: While in near stoichiometric LN the first domain reversal and the reverse poling process require almost the same coercive field strength, in congruent LN the two field strengths differ. This is directly related to polar defect clusters, which do only incompletely reverse during domain inversion, resulting in a built-in electric field opposing the spontaneous polarization [11]. In addition, due to slower screening and the built-in field, congruent LN is more prone to flip back into its original polarization upon removal of the switching field [11]. To overcome these challenges, a relatively high magnesium doping concentration of 4.5 to 5 mol% [13] can be added to the growth melt without adding much complexity in crystal growth or handling of the resulting wafers. Therefore, Mg-doped wafers are equally common as congruent wafers. To illustrate the different poling behavior of congruent and Mg-doped LN, we performed domain-engineering-related experiments, the results of which are depicted in Fig. 1: (a) and (b) are related to congruent LN, while (c) and (d) to 5%-Mg-doped LN.

More precisely, Fig. 1(a) shows a plot of a typical ferroelectric hysteresis loop taken on an approximately 500-μm-thick monodomain crystal of congruent LN. The crystal was contacted via an electrolyte solution of water and lithium chloride in a large area, while the high voltage was supplied by a high-voltage amplifier (Trek 20/20) coupled to a computer with an AD/DA card for output and current monitoring. Here, a very large coercive field strength of $22 \pm 0.5\ \frac{kV}{mm}$ is required for the initial reversal of the as-grown, monodomain crystal. Interestingly, reversing this poling again requires only a field

*Contact author: adriana.bocchini@upb.de

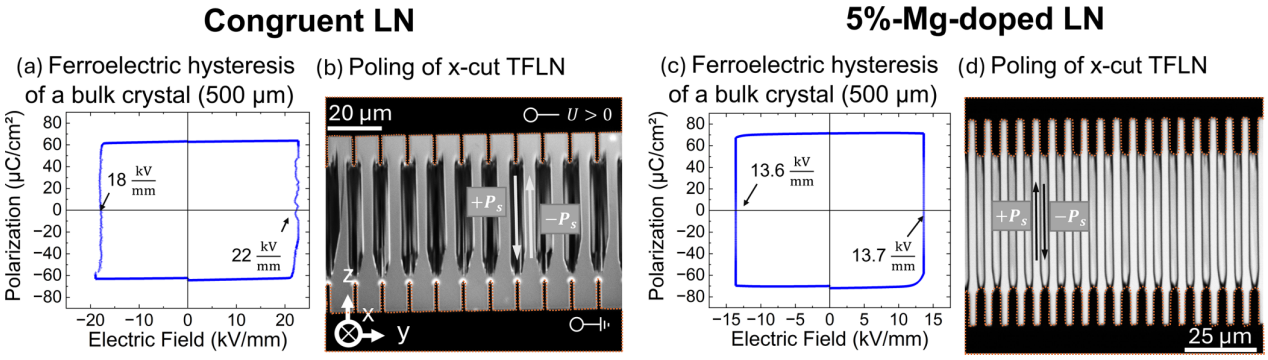


FIG. 1. Examples for the impact of Mg-doping on different aspects of domain engineering: Doping a congruent crystal with Mg lowers the coercive field, which is seen in the hysteresis loops taken on 500-µm-thick, *z*-cut, single-domain crystals of (a) congruent vs (c) a 5%-Mg-doping concentration. In addition, SHGM pictures of periodic-poling experiments on *x*-cut thin-film lithium niobate (TFLN) show a much less regular domain structure for the (b) congruent vs (d) a 5%-MgO-doped sample. Here, the dashed, orange outline indicates the deposited finger electrodes to which a single poling pulse of sufficient height to overcome the coercive field was applied.

of $18 \pm 0.5$ $\frac{\text{kV}}{\text{mm}}$. Both values match well with established literature values [9,11,14,15]. Here, both the difference in forward and backward poling, as well as the very large field required for poling, is related to the charged defect clusters formed by Li vacancies and Nb-antisite defects discussed above. In contrast, for (near-)stoichiometric LN crystals, coercive fields of 5 $\frac{\text{kV}}{\text{mm}}$ or lower are reported [9,11,14]. On the other hand, for Mg-doped LN the ferroelectric hysteresis shows a reduction of coercive field to about $13.5 \pm 1$ $\frac{\text{kV}}{\text{mm}}$ compared to congruent LN and an almost symmetric behavior for forward and reverse poling indicating a lower polar defect concentration [11], see Fig. 1. Even lower coercive field strengths down to 6 $\frac{\text{kV}}{\text{mm}}$ are reported in literature for 5%-Mg-doped LN, which depends on exact doping and stoichiometry [9,16].

Apart from the coercive field strength, the composition also influences the stability of the domain walls and the domain itself. Domain walls act like traps for (charged) defects [17]. An example is shown in Fig. 1(b), which shows a second-harmonic generation microscopy (SHGM) image of a periodically-poled 600-nm-thick, *x*-cut, thin-film of congruent LN (TFLN) on an insulator. The poling experiments for the thin films were performed via metal finger electrodes deposited on the surface of the *x*-cut crystal, similar to Refs. [18–20]. Here, SHGM is very sensitive to the domain structure in thin-film LN, where ideal domain walls would appear as black lines separating the domains [21]. However, the image of the congruent film, overall, shows an irregular domain structure with grayish domains and nonstraight domain walls. This is probably due to weak pinning of domains or domain walls [11]. It should be noted that the thin films are fabricated via ion slicing [1], which might introduce additional defects or different defects from bulk *z*-cut congruent domains, further adding to the challenge of poling.

In addition, the Mg doping also improves the overall domain structure homogeneity, as clearly visible from the SHGM image shown in Fig. 1(d), related to a 600-nm-thick, *x*-cut, 5%-Mg-doped-LN thin film. Here, it can be seen that the domains and domain walls appear to be much straighter and symmetric, indicating that the Mg-doping improves pinning or stabilization of the domains and domain walls. Besides, the doping is known to impact various other properties, e.g., it is established that MgO-doping also drastically enhances the damage threshold against the photorefractive effect [9].

MgO-doped LN crystal can be fabricated over a wide range of dopant concentrations. However, most of the beneficial effects, like drastically lower photorefraction, only appear at a threshold of approximately 4.5–5 mol% doping concentration [13]. Therefore, the most commonly available doping concentrations are around 5 mol% for commercial crystals. It is noteworthy, however, that the performance of LN in devices is again impaired for Mg concentrations higher 10 mol%, e.g., due to an increased photorefractivity or a poor poling behavior.

It is commonly believed that the beneficial role of Mg dopants in LN consists of replacing the Nb antisite defects. As proposed by Iyi *et al.* in Ref. [22], the incorporation of different concentrations of Mg in LN crystals is a complex process involving a concentration-dependent change in the site occupation, the formation of charge-compensating Li vacancies, and a variable $\frac{[\text{Li}]}{[\text{Nb}]}$ ratio. In addition, some authors also propose the formation of compensating Nb vacancies [23]. In the literature, plenty of works on the incorporation of Mg in LN can be found, focusing both on its beneficial effect and structural properties. Nevertheless, the role of different Mg concentrations during poling, and the reason why high concentrations of Mg are detrimental for the crystals' properties, are far from being completely understood.

This motivates the present work in which we apply density functional theory (DFT) to model Mg-doped LN crystals, considering different (i) doping concentrations, (ii) site occupations, and (iii) distances between dopants. For each concentration, we then determine the energetically most favorable defect geometry, computing its formation energy at different charge states. In addition, we use the nudged elastic band (NEB) method [24] to characterize the dopants' impact on the coercive field strength. By this, we expect to clarify the picture of the role of Mg during domain inversion.

## II. COMPUTATIONAL DETAILS

Calculations are performed under periodic boundary conditions in the framework of DFT as implemented in the

open-source program package QUANTUM ESPRESSO (QE) [25,26]. During the calculations, we use norm-conserving pseudopotentials, and wave functions are expanded into plane waves up to an energy cutoff of 85 Ry. In addition, in all the calculations, the Brillouin-zone sampling is restricted to the Baldereschi point [27] to reduce the computational effort so that the required comprehensive study of plenty of different defect concentrations and configurations becomes possible.

For the description of the electronic exchange and correlation (XC) effects, we use the generalized gradient approximation (GGA) via the PBEsol [28,29] functional. The inclusion of the Hubbard correction [30] (DFT + $U$) improves the description of strongly localized niobium (Nb) 4$d$ (defect) states. The Hubbard correction (i.e., the so-called Hubbard $U$) is included following the simplified scheme by Cococcioni and de Gironcoli [30]. This correction improves the description of the strongly localized Nb 4$d$ orbitals, and, thus, allows for an accurate description of defect-stabilized electrons (or holes) at a lower computational cost compared to the application of, e.g., hybrid functionals. The magnitude of the Hubbard $U$ is self-consistently [30] determined in the stoichiometric LN unit cell, and matches with those of previous studies on LN [31–33]. Although the magnitude of the $U$ parameter is to some extent influenced by the positioning and the local environment of the Nb in the LN cell [31], for the sake of simplicity, in this work we neglect the possible influence of Mg dopants on the magnitude of the Hubbard correction and apply the values of $U = 4.7$ eV and $U = 5.2$ eV for the $Nb_{Nb}$ and the $Nb_{Li}$, respectively, irrespective of their local environment.

The starting point of our calculations consists of the stoichiometric, rhombohedral LN unit cell composed of two Li, two Nb, and six O atoms. This cell is then doubled along each lattice direction, resulting in a larger 80-atom supercell. As described in Refs. [31,34], this supercell size allows for an accurate modeling of the congruent composition (i.e., $\frac{[Li]}{[Nb]} = 0.94$) by the introduction of a Nb antisite in the charge state +4 (i.e., $Nb_{Li}^{4+}$) and neglecting the formation of charge compensating Li vacancies, yielding the ratio $\frac{[Li]}{[Nb]} = 0.88$.

During the geometry relaxation, we optimize the atomic positions, while the lattice dimensions are kept at their experimental values [35]. This procedure allows for the simulation of (quasi-)noninteracting, isolated point defects. The atomic positions are relaxed until residual forces and energy fluctuations are lower $10^{-8}$ Ry/Bohr and $10^{-4}$ Ry, respectively.

To systematically investigate the influence of different concentrations of magnesium (Mg) dopants on the poling behavior, we substitute up to three Nb and/or Li sites with Mg, i.e., either only Li ($Mg_{Li}$) or Nb ($Mg_{Nb}$) substitutional atoms or a combination of both, to investigate (i) how the site positioning of the Mg dopants impact on the properties of LN and (ii) the effects arising from the distance between two dopants. In addition, for each concentration, we simulate different nonequivalent configurations.

The relative Mg concentration $C_{Mg}$ is determined as [23]

$$C_{Mg} = \frac{[MgO]}{[LiNbO]_3 + [MgO]} = \frac{[Mg]}{[Li] + [Nb] + [Mg]}. \quad (1)$$

Mg dopants are discussed to be charge compensated by intrinsic defects, such as Li or Nb vacancies [23]($V_{Li}^{-}$ and $V_{Nb}^{4+}$, respectively), or defect clusters (e.g., $Mg_{Nb}^{3+} + OH$ [36]). Their modeling, however, requires the use of rather large supercells [37] to reduce artifacts caused by the application of periodic boundary conditions. So, due to the large number of different defect combinations and concentrations, we do not simulate these compensating defects directly, but discuss the relative thermodynamic stability of different Mg-dopant configurations via the formation energy of differently charged defects. Keeping in mind the neglected charge compensating vacancies, each introduced substitutional increases the Mg concentration in the supercell by 3.125%. As a consequence, the two threshold concentrations of about 4.5% and 10% can be approximated by the modeling of one to three substitutionals (i.e., 3.125 mol%, 6.250 mol%, and 9.375 mol%), yielding a comprehensive picture of the Mg-doping mechanisms. We note that both the stoichiometric as well as the congruent compositions correspond to nominally Mg-undoped crystals (i.e., 0 mol%).

The defect formation energy $E_{form}^{q}$ of a $q$-fold charged defect as a function of the Fermi level $\varepsilon_F$ is defined as [38–40]

$$E_{form}^{q}(\varepsilon_F) = E_{def} - E_{ideal} - \sum_i n_i \mu_i + q[\varepsilon_F + E_{corr}], \quad (2)$$

with $E_{def}$ as the ground-state energy of the supercell containing point defects, $E_{ideal}$ as the energy of the ideal supercell, $n_i < 0$ the number of atoms subtracted ($n_i > 0$ if added) from (to) the supercell, and $\mu_i$ the chemical potential of the respective elements. The chemical potentials for Mg, Li, and Nb required here are determined via the ground-state energies of bulk MgO, $Li_2O$, and $NbO_2$, respectively, using the energy of one O atom in molecular $O_2$ corrected by −0.27 eV [41] to account for room temperature and normal pressure as a reference. We would like to point out that since in the following we do not compare systems with different Mg concentrations, the results here discussed do not depend on the Mg chemical potential. $E_{corr}$ represents various energy corrections required to compensate for, e.g., finite-size or charge effects. To avoid possible inaccuracies from the explicit choice of these corrections, we applied the so-called Slater-Janak transition-state model [42–44]. In this framework, the formation energy is computed via Eq. (2) for the neutral cell (i.e., $q = 0$), which renders energy corrections unnecessary. The charge transition levels ($N/N+1$) are directly determined from half-filled one-particle levels as

$$(N/N+1) = E^{N+1} - E^{N} = \int_0^1 \varepsilon_H(\eta)\, d\eta = \varepsilon_H\left(\frac{1}{2}\right). \quad (3)$$

Here, $E^{N+1}$ and $E^{N}$ indicate the energies of a supercell containing $N+1$ and $N$ electrons, respectively, and $\varepsilon_H(\eta)$ stands for the one-particle energy (with respect to the VBM) of the highest Kohn-Sham orbital affected by the charge transition $N \rightarrow N+1$. Thus, Eq. (3) clearly shows that within this formalism, the charge transition states do not depend on the total energy of the cells, but only on the relative position of Kohn-Sham one-particle energies, which are less influenced by electrostatic interactions in the cells, rendering the application of total-energy corrections obsolete.

Finally, for the energetically most favorable defect geometries and charge states, we perform nudged-elastic band (NEB) calculations [24] to investigate how Mg dopants influence the coercive field strength. Here, a force convergence criterion of 0.05 eV/Å is used. All other convergence criteria remain unchanged.

The so-obtained results are discussed in the following sections: In Sec. III A, we discuss the influence of different Mg-doping concentrations and relative distances between dopants at different lattice sites on the structural properties of LN. In addition, we determine the energetically most favorable configuration for each defect concentration and combination of $Mg_{Li}$ and $Mg_{Nb}$ substitutionals by comparing the ground-state energies of equiatomic cells. In Sec. III B, we discuss the defect formation energy of the so-determined most favorable structures with respect to the Fermi-level position. Finally, in Sec. III C, we compute the activation barriers for the inversion to understand how the dopants influence the coercive field strength and the poling process itself.

## III. RESULTS AND DISCUSSION

### A. Defect geometries

As already discussed in Refs. [45,46], the energetically most favorable charge states for the $Mg_{Li}$ and $Mg_{Nb}$ substitutionals correspond to completely emptied and filled defect levels, respectively. The former behave as electron donors, while the latter behave as electron acceptors, yielding $Mg_{Li}^{+}$ and $Mg_{Nb}^{3-}$. This finding allows us to reduce the computational effort: We use these charge states to evaluate the relative stability of the reasonable defect configurations for each examined defect concentration, giving insight into how the dopants are distributed within the LN lattice.

Though, since the technologically most relevant LN stoichiometry corresponds to the congruent composition, and the beneficial effects of Mg dopants are discussed to arise from a replacement of $Nb_{Li}$ with $Mg_{Li}$, we do not only compare the impact of the dopants to the properties of stoichiometric LN, but also to those of a crystal showing a congruent composition. As visible in Fig. 2(b), the Nb antisite does not significantly alter the overall appearance of the supercell, whereby the reduction of the $Nb_{Li}^{4+}O_6$ cage volume by about 17% (i.e., $Vol_{LiO_6} = 12.36\,Å^3 \rightarrow Vol_{Nb_{Li}O_6} = 10.25\,Å^3$) is the most visible change. However, as already pointed out in Ref. [47], the antisite provokes a slight disorder in the Li sublattice (i.e., the distance $d$ between a Li site and its neighboring Nb atom changes slightly compared to the value in the stoichiometric case, see also Fig. 2), especially along the polyhedra chain in which the $Nb_{Li}^{4+}$ has been placed.

The easiest scenario for the Mg doping corresponds to a single Mg substituting for either one Li or one Nb site in the stoichiometric LN supercell. This yields a local [Mg] concentration of 3.125 mol% in the supercell. Also the Mg dopant on the Li site does not significantly alter the overall appearance of the supercell: Compared to the antisite, $Mg_{Li}^{+}$ reduces slightly the disorder of the Li sublattice, while the volume of the $Mg_{Li}^{+}O_6$ cage is enlarged, deviating only by about 3.7% from the stoichiometric cell (i.e., $Vol_{LiO_6} = 12.36\,Å^3 \rightarrow Vol_{Mg_{Li}O_6} = 12.30\,Å^3$). In the case of $Mg_{Nb}^{3-}$, on the other hand, the distance between the Mg dopant and the closest Li atom is reduced by about 4.9%. Similar observations have also been reported and attributed to electrostatic interactions in Ref. [45].

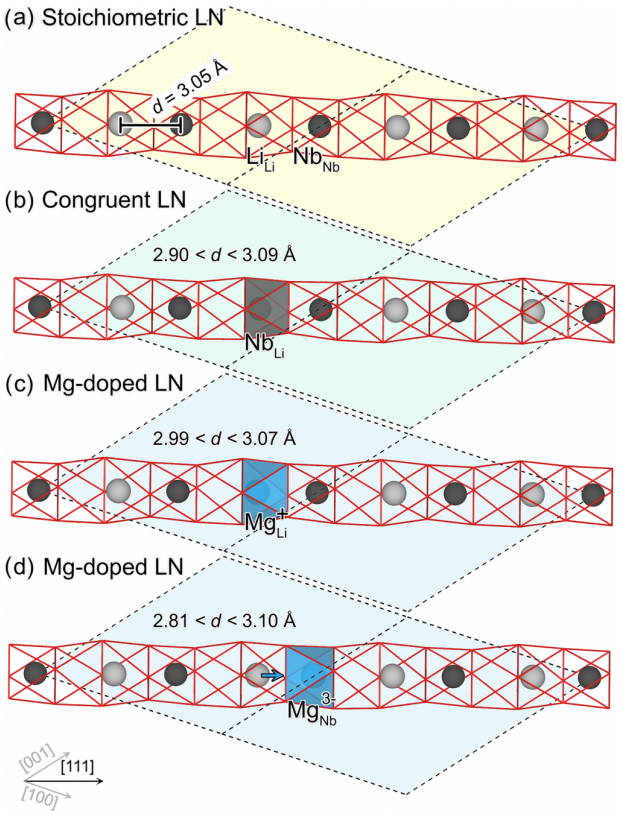


FIG. 2. Geometries of (a) an 80-atom stoichiometric LN supercell, (b) an 80-atom LN supercell with a congruent composition, (c) and (d) an 80-atom LN supercell containing one $Mg_{Li}^{+}$ and a $Mg_{Nb}^{3-}$, respectively, yielding a concentration of [Mg] = 3.125% in the supercell. For clarity, only the polyhedra chain containing the defect (parallel to the $z$ axis, i.e., the [111] crystal direction) is shown. Light, dark, and cyan balls indicate Li, Nb, and Mg atoms, respectively. The red sticks represent the oxygen cages. The supercell size is hinted at by the dashed box.

Apart from the combination of a $Mg_{Li}^{+}$ and one $Mg_{Nb}^{3-}$ [45], the microscopic structure of higher Mg-doping concentrations has not been systematically investigated, yet. To gain a thorough picture of the Mg incorporation in LN, we thus model supercells with a nominal concentration of [Mg] = 6.250 mol% and [Mg] = 9.375 mol%. For this, we model supercells featuring two and three substitutionals, respectively. For their relative placement, there are plenty of possibilities. To this end, we model not only defect cells containing single $Mg_{Li}^{+}$ or $Mg_{Nb}^{3-}$, but also combinations of both kind of dopants with varying relative positions within the 80-atom supercell.

We note that the defect configurations here modeled, however, are not expected to directly reflect the overall, macroscopic structure of real LN crystals highly doped with Mg. Nonetheless, they are crucial to understanding how local Mg-dopant accumulations could influence the poling behavior.

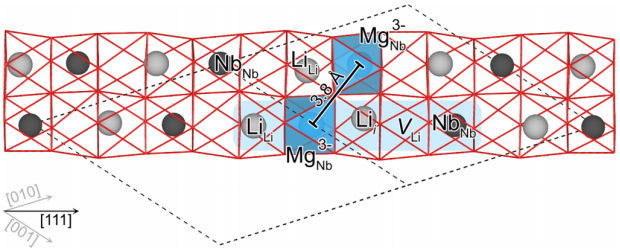


FIG. 3. If two $Mg_{Nb}^{3-}$ substitutionals are located at nearest-neighbor-Nb distance (in this case about 3.8 Å), one near Li atom is shifted into an adjacent empty cage. Note that this configuration is energetically unfavorable (about 1 eV less favorable compared to the most-favorable configuration).

For [Mg] = 6.250 mol%, we modeled five and seven different configurations for two $Mg_{Li}$ ($Mg_{Nb}$) and the mixed case, respectively. We find that $Mg_{Li}$ tends to be uniformly distributed within the supercell, since all the simulated configurations are almost degenerate with respect to the total energy. The ground states of the structures, in fact, deviate less than 100 meV from each other, whereby structures in which the substitutionals are located in the same polyhedral chain are slightly less favorable.

When two $Mg_{Nb}$ are implanted in the crystal, differences in the total energy of different configurations are more pronounced, i.e., up to 1.1 eV. More precisely, we find that the defect configurations are energetically more favorable for intermediate distances between different $Mg_{Nb}$ in the cell: The most favorable geometry corresponds to the one in which the $Mg_{Nb}^{3-}$ are inserted in two consecutive Nb sites located in the same polyhedra chain parallel to the $z$ axis, i.e., $Li_{Li}Mg_{Nb}V\ Li_{Li}Mg_{Nb}$. The two energetically least favorable configurations, on the other hand, correspond to the one with the largest and the lowest value of $\overline{Mg_{Nb}Mg_{Nb}}$ distance, i.e., about 7.5 Å and 3.8 Å, respectively. The former corresponds to the scenario where both substitutionals are located in the same polyhedra chain at crystallographically equivalent lattice sites. When one Li and one Nb site are substituted with Mg (i.e., $Mg_{Li}^{+1} + Mg_{Nb}^{3-}$), the ground states of all the simulated configurations are relatively close in energy with a maximum deviation of about 0.3 eV.

Regarding the impact on the local structure, the following trends are recognized:

(i) In the case of two $Mg_{Li}^{+}$ dopants, we find again that the atomic positions inside the supercell remain almost unaffected.

(ii) Although isolated $Mg_{Nb}$ have a minor impact on their local environment, when two $Mg_{Nb}$ are located closer than 3.8 Å, a strong disorder in the local Li sublattice is obtained: In the final structure, in fact, the two dopants still reside at ideal Nb sites, but are surrounded by three Li atoms yielding a $Li_{Li}Mg_{Nb}Li_iV_{Li}Nb_{Nb}$ occupation of the polyhedral chain, also see Fig. 3.

(iii) For the combined case, a mixture of both trends is observed. $Mg_{Li}^{+}$ has little influence on neighboring atoms, while $Mg_{Nb}^{3+}$ attracts the surrounding Li atoms.

According to our calculations, $Mg_{Nb}$ is suggested as a driving force behind the reported defect aggregation, whereby

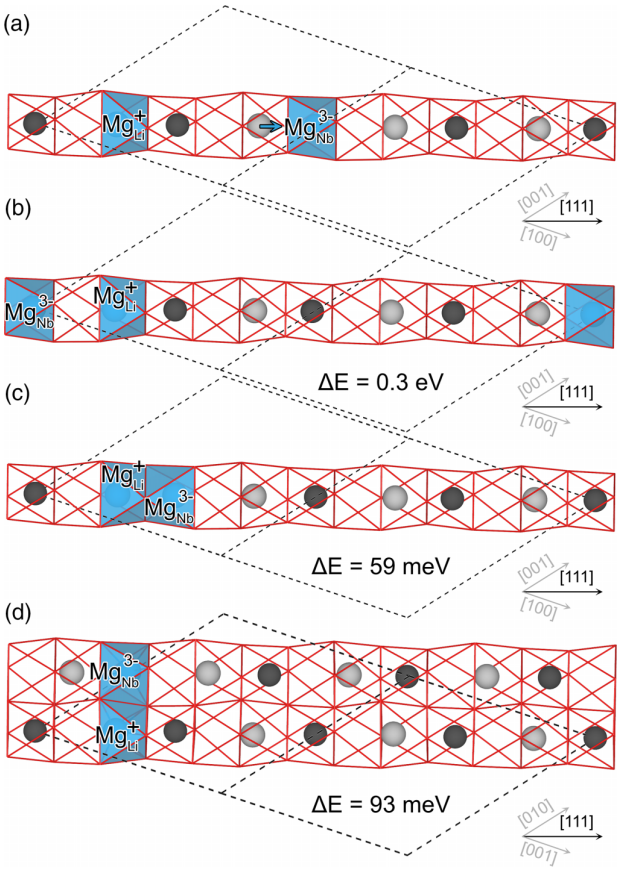


FIG. 4. (a) The energetically most favorable configuration for a combination of one $Mg_{Li}^{+1}$ and $Mg_{Nb}^{3-}$ is achieved when they are located in the same polyhedral chain at an intermediate distance, (b) the least favorable (about 0.3 eV) configuration of the ones we simulated is obtained when the two substitutionals are separated by one empty cage. The configurations in which the $Mg_{Li}$ and the $Mg_{Nb}$ are located are only by 59 meV (c) and 93 meV (d) less favorable compared to the structure shown in (a). Notably, structure (b) would correspond to structure (c) after domain inversion.

the combination of $Mg_{Nb}$ and $Mg_{Li}$ substitutionals plays a major role in the determination of the poling behavior. For example, we find that the energetically second most favorable configuration basically corresponds to the geometry of the least favorable ones after poling, also see Figs. 4(b) and 4(c). This aspect is discussed in more detail in Sec. III C. Our results thus confirm previous reports [36], which found that the combination of three $Mg_{Li}$ with one $Mg_{Nb}$ causes strong lattice deformations.

To simulate our highest doping concentration [Mg] = 9.375 mol%, we modeled nine different configurations for three $Mg_{Li}^{+}$ ($Mg_{Nb}^{3-}$), and 18 for the case of two $Mg_{Li}^{+}$ combined with one $Mg_{Nb}^{3-}$ (one $Mg_{Li}^{+}$ with two $Mg_{Nb}^{3-}$).

After substituting three atoms in the cell, the same, but more pronounced effects as previously discussed can be observed:

(i) The replacement of only Li sites leads to barely any local structural change, and again all the simulated structures are very close in energy (i.e., with deviations lower 200 meV),

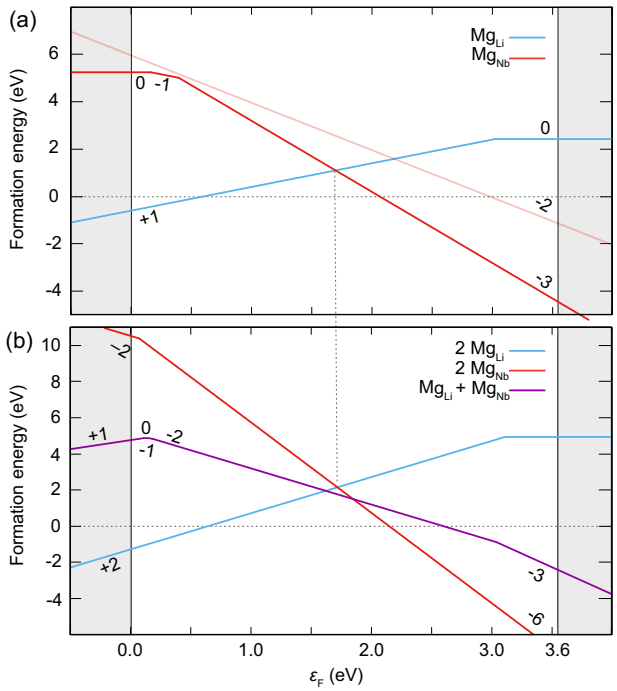


FIG. 5. Formation energy of different concentrations of Mg dopants, i.e., (a) [Mg] = 3.125 mol% and (b) [Mg] = 6.250 mol%. Only the energetically most favorable defect geometries discussed in Sec. III A are considered.

whereas the structures tend to be more favorable if the $Mg_{Li}^{+}$ are located in different polyhedral chains.

(ii) Again, for $\overline{Mg_{Nb}Mg_{Nb}}$ distances below 4 Å, the replacement of Nb sites causes strong lattice deformations; additional Li atoms are attracted, and simultaneously quasi-isolated Nb atoms are left behind in the lattice. These configurations, however, are highly unfavorable (up to 2.2 eV).

(iii) If both Li and Nb atoms are exchanged with Mg, again, the stability of the configuration depends on the relative positioning (site occupation) as well as the distance between dopants.

The final geometries for this high defect concentration, however, are not expected to reflect the global morphology of extended LN crystals heavily doped with Mg. Our models are rather meaningful to characterize local defect clusters, which could spontaneously form within these crystals, and could be instrumental in explaining the impaired properties of LN crystals reported for Mg-doping concentrations above the second threshold level.

### B. Formation energy

For the energetically most favorable defect configuration discussed in Sec. III A, we compute the formation energy with respect to their charge state as a function of the Fermi level $\varepsilon_F$. The so-obtained curves are shown in Fig. 5. In contrast to Ref. [45], the superposition of the spin-polarized defect states is modeled here using high-spin configurations. This choice is reasonable since both the antiferromagnetic and the diamagnetic spin configuration for the neutral structure shown in Fig. 4(c) are by 235 meV and 53 meV, respectively, energetically less favorable compared to the same structure in the high-spin configuration. To our knowledge, only the formation energy of one isolated Mg substitutional has already been discussed in the literature (see Refs. [45,46]). Here, 120-atom conventional supercells have been used, resulting in a doping concentration of [Mg] $\approx$ 2.1 mol%. Thereby, Li *et al.* [45] utilized hybrid functionals to improve the description of localized charges (here, we apply the Hubbard correction), and also discussed the interactions between dopants and Li vacancies. On the other hand, Kong *et al.* [46] examined the charge states $Mg_{Nb}^{3-}$ and $Mg_{Li}^{+}$, exclusively, and studied the co-doping with zirconium (Zr). Our results for one substitutional [see Fig. 5(a)] are in good agreement with both studies [45,46]. However, due to the application of hybrid functionals, which also leads to an enlarged fundamental band gap, the positions of the charge transition states discussed in Ref. [45] occur at larger energies. Nevertheless, all studies indicate $Mg_{Li}^{+}$ to be most favorable for Fermi energies in the lower half of the band gap, while $Mg_{Nb}^{3-}$ is predicted to be stable for higher positions. So, considering experimental Nb-rich growing conditions, the former is more likely to be found in real crystals. In addition, only the charge states not featuring unpaired electrons are predicted to be thermally stable.

A similar picture holds for supercells containing two substitutionals, see Fig. 5(b). Again, Mg substitutionals on Li sites are predicted for lower Fermi energies, those on Nb sites for higher positions. On the other hand, a combination of both types is energetically favorable for intermediate positions. Notably, the transition between two $Mg_{Li}^{+}$ and the combination of one $Mg_{Li}^{+}$ and one $Mg_{Nb}^{3+}$ happens at a slightly lower Fermi level. Thus, considering that for this doping concentration already the end of Nb-rich conditions could be reached, our data are in agreement with the current model allowing for the formation of $Mg_{Nb}$ for concentrations higher than 5%.

Here, we refrain from systematically computing the formation energy of supercells showing higher concentrations of [Mg]. Nevertheless, we would like to point out that some test calculations show that the relevant transition state between the energetically most favorable supercell containing three $Mg_{Li}$ substitutionals and the most favorable one containing two $Mg_{Li}$ and one $Mg_{Nb}$ is shifted toward even lower Fermi-level positions. Thus, the formation of Nb substitutionals appears to be even likelier in heavily Mg-doped LN crystals.

### C. Activation energy

It should be stressed that the domain inversion is a highly dynamical process, where time-dependent charge transport of the depolarization charge of the lattice and the associated screening charges, as well as pinning and propagation of domain walls, play an important role in the poling dynamics [48–51]. This includes, for example, the transport of screening charges from the $z$ surfaces of the crystal upon domain inversion, the pinning of domain walls to defects, as well as the propagation of charged head-to-head or tail-to-tail domain walls, as well as their screening during domain growth. However, due to the nature of our model, these effects play no role, because on the one hand, the periodic boundary conditions result in an effectively infinite crystal with no

TABLE I. Experimental coercive field strengths and DFT energy barriers for the poling process of stoichiometric LN (sLN), congruent LN (cLN), and Mg-doped LN [9,11,14,15,57]. For congruent LN the poling process of a previously reversed crystal requires a lower coercive field compared to as-grown crystals [11].

| Experiment [9,11,14,15,57] | | | Theory | | |
|---|---|---|---|---|---|
| Composition | Coerc. field, as-grown $\left(\frac{\text{kV}}{\text{mm}}\right)$ | Coerc. field, reversed $\left(\frac{\text{kV}}{\text{mm}}\right)$ | Defect model | Barrier, as-grown (eV) | Barrier, reversed (eV) |
| sLN | ≈4 | ≈4 | sLN | 1.23 | 1.23 |
| cLN | ≈21 | ≈16−17 | $Nb^{4+}_{Li,\,AB}$ | 1.70 | 1.70 |
| | | | $\left(Nb^{4+}_{Li,\,AC}\right)$ | (1.06) | (0.20) |
| [Mg] ≈ 2.5 mol% | ≈17 | ≈12 | $Mg^{+}_{Li}$ | 1.42 | 1.42 |
| | | | $Mg^{3-}_{Nb}$ | 0.67 | 0.67 |
| [Mg] = 5 mol% | ≈13 | ≈12 | Two $Mg^{+}_{Li}$ | 1.12 | 1.12 |
| | | | $Mg^{+}_{Li}$+$Mg^{3-}_{Nb}$ | 0.78 | 0.52 |
| | | | Two $Mg^{3-}_{Nb}$ | 0.57 | 0.57 |
| [Mg] = 7.5 mol% | ≈12 | ≈10 | | | |

charged interfaces. Notably, some recent studies [52–56] have shown that even in the presence of domain boundaries modeled under periodic conditions, screening effects do not have to be accounted for, since they cancel out each other when both tail-to-tail and head-to-head configurations are modeled. For a realistic modeling of domain walls and the description of domain propagation, larger supercells as the ones used in the present studies, as well as time-dependent techniques like molecular dynamics (MD), are required [52–56]. These, however, would go clearly beyond the scope of this work. Nevertheless, the influence of Mg doping on the poling behavior of LN can already be seen from nudged elastic band (NEB) calculations, allowing us to determine the energy barriers, which have to be overcome during the inversion. They, in fact, can be used as points of comparison, since the energy barriers are correlated with the coercive field strength. Stoichiometric LN is characterized by rather low coercive fields, see Table I [9,11,14] making the domain inversion easier. Although it should also be noted that this does not necessarily mean that the domain and domain wall stability are improved. In contrast, the domain inversion in the widely used congruent composition is very challenging due to the very large required fields. Further, the field is significantly different for an as-grown crystal and an already reversed one, which is an indication of charged defect dipoles not inverting during poling [11]. On the other hand, it was found [16] that increasing the Mg content up to 6.5 mol% reduces five-fold the magnitude of the switching field compared to the one required to pole congruent LN.

Before discussing the influence of Mg dopants on the energy barriers, we investigate the barriers of stoichiometric and congruent LN to get a reference point, see Figs. 6(a) and 6(b), respectively. As expected, the inverted stoichiometric LN supercell is energetically degenerate with the unpoled one. This results in a symmetric pathway during poling, whereby an energy barrier of about 1.23 eV has to be overcome, also see Fig. 6(a). This is in agreement with experimental observations that the internal defect fields are close to zero in stoichiometric LN, and the same field strength is observed for poling an as-grown crystal and for the reversal to the original state.

In the case of congruent LN, on the other hand, there are two possible scenarios to model the poling process: (i) only the $Li_{Li}$ are shifted into the adjacent empty $O_6$ cage, while the Nb antisite is left at its original position [see structure C in Fig. 6(b)] and (ii) all the atoms occupying a Li site are shifted, in particular also the $Nb_{Li}$ [see structure *B* in Fig. 6(b)]. Although the latter features a higher activation energy (and, as a consequence, a higher coercive field), it is closely related to one of the stoichiometric cells. On the other hand, since structure *C* is energetically less favorable compared to the original structure *A*, the taken pathway is not symmetric, whereas the activation energy from $A \rightarrow C$ is by about 0.5 eV higher compared to the opposite direction. This observation is in agreement with the defect model discussed by Gopalan *et al.* [11]. In addition, structure *C* is characterized by a strong disorder in the Li sublattice, see Fig. 6. We propose that the challenges of the poling process in congruent LN originates from exactly this disorder, as well as the low activation energy from $C \rightarrow A$, which could promote the backflipping of the crystal into its original polarization and, therefore, result in an unpoled crystal. Spontaneous backflipping is a phenomenon well known in congruent LN crystals [14,58]. In agreement with experimental observations of the coercive fields, the congruent composition shows a higher activation energy compared to the stoichiometric one.

The poling process of Mg-doped LN, on the other hand, is a complex process, possibly involving intermediate states. Thus, to simplify the description of the poling process, we decide to focus on the discussion of the completely inverted material, i.e., those configurations in which every atom located at a Li site (i.e., $Li_{Li}$ and $Mg_{Li}$) is shifted into the adjacent empty $O_6$ cages. We briefly note, however, that it is also possible to shift all the $Li_{Li}$, but leaving the position of the $Mg_{Li}$ unchanged. On the contrary, we find that shifting one single Li atom into an empty cage is only possible for an adjacent $Mg_{Nb}$ (i.e., leading to the following sequence $Li_{Li}Mg_{Nb}Li_iV_{Li}Nb_{Nb}$), otherwise it would relax back into its original position. The $Mg_{Li}$, on the other hand, can be individually moved. We thus propose that $Mg_{Li}$ is not only helpful to suppress the formation of the Nb antisite and, by

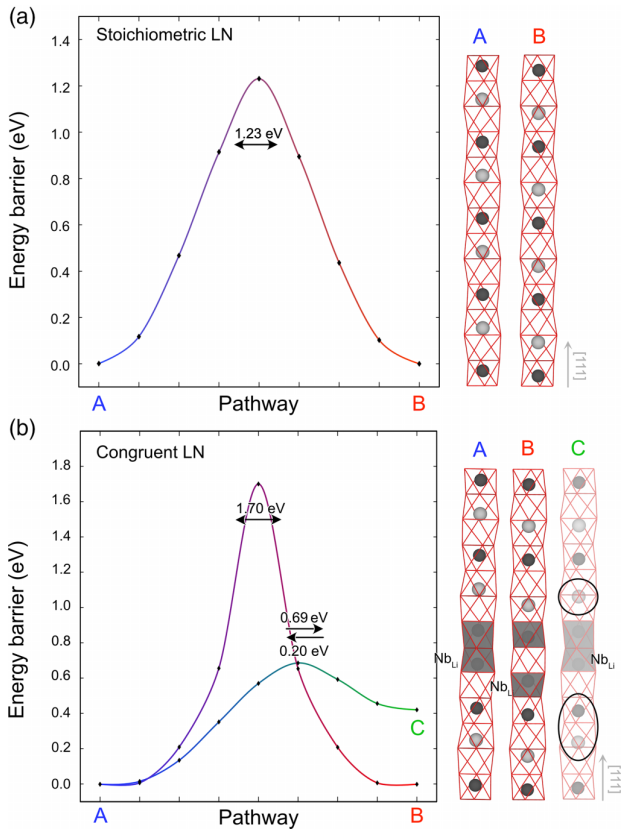


FIG. 6. Energy barriers, which have to be overcome to pol (a) stoichiometric LN and (b) congruent LN. Note that for congruent LN there are two possibilities to simulate the poling process: (i) only shift the position of all the $Li_{Li}$ in the supercell (see structure C) or (ii) all the Li sites irrespective of the occupation (i.e., also the $Nb_{Li}$ is shifted into the adjacent cage, structure B). The former is characterized by a lower activation energy, but it features a strong disorder in the Li sublattice.

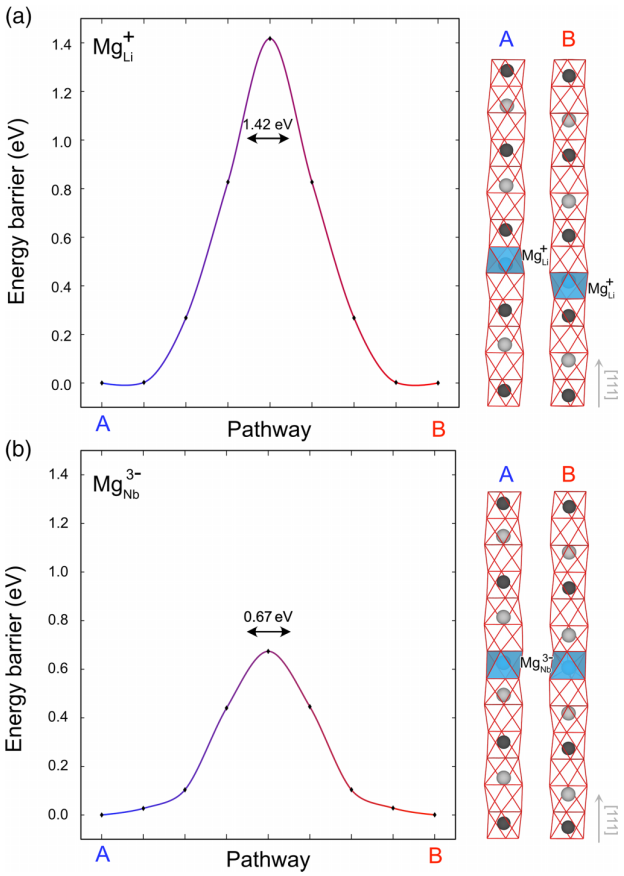


FIG. 7. Activation energies of the poling process for Mg-doped LN with [Mg] = 3.125 mol%. More precisely, the cells containing one single $Mg^{+}_{Li}$ and one single $Mg^{3-}_{Nb}$ are shown in (a) and (b), respectively.

this, its negative influence on the poling process as previously discussed, but they could also act as a seeding point for the domain inversion. This is an interesting observation, as some experimental works propose the beneficial effect of applying electric 'wake-up' pulses below the coercive field, before applying the actual poling pulse [59]. The 'wake-up' pulses may first move some of the $Mg_{Li}$ atoms, which makes the subsequent movement of other ions, like Li, easier. For a conclusive picture of this effect, however, additional experimental and theoretical investigations are required.

The energy barriers computed for the energetically most favorable defect geometry for one Mg substitutional are compiled in Fig. 7. The activation energy for the supercell containing one single $Mg_{Li}$ amounts to 1.42 eV, which, although being slightly higher are the one for stoichiometric LN, reflects the experimental finding that compared to the congruent composition the magnitude of the coercive field decreases after the Mg doping. In fact, the barrier is 16.5% lower than the one in congruent LN. In addition, the shape of the curve is symmetric, since we only simulate the fully reversed configuration. If the position of the substitutional or of all the $Li_{Li}$ would be shifted, the end structure (and thus its ground-state energy) would differ from that of the pristine structure, yielding an asymmetric line shape and different activation energies depending on the chosen reaction direction.

The energy barrier is even lower in the case of one single $Mg_{Nb}$, i.e., about 0.67 eV. We think that this is caused by electrostatic interactions between the negatively charged $Mg^{3-}_{Nb}$ and the positively charged $Li^{+}$ ion, which (as described in Sec. III A) also leads to a reduced distance between the Mg and the adjacent Li compared to the distance $\overline{NbLi}$ in the stoichiometric material.

At first sight, one could thus think that $Mg_{Nb}$ are required to see an improvement of the poling characteristics of LN. However, both the defect formation energy as well as Raman measurements [60] indicate $Mg_{Li}$ to be the main defect in technologically relevant Mg-doped LN.

Moreover, when higher doping defect concentrations are considered, the presence of $Mg_{Nb}$ actually turns out to be detrimental during poling, see Fig. 8. This holds especially for the combination of substitutionals on different crystallographic sites, which are the most probable, considering that the formation of Mg substitutionals on Nb sites is restricted to the presence of Mg substitutionals on Li sites, see Fig. 5(b). In fact, the ground-state energy (and therefore the energy barrier)

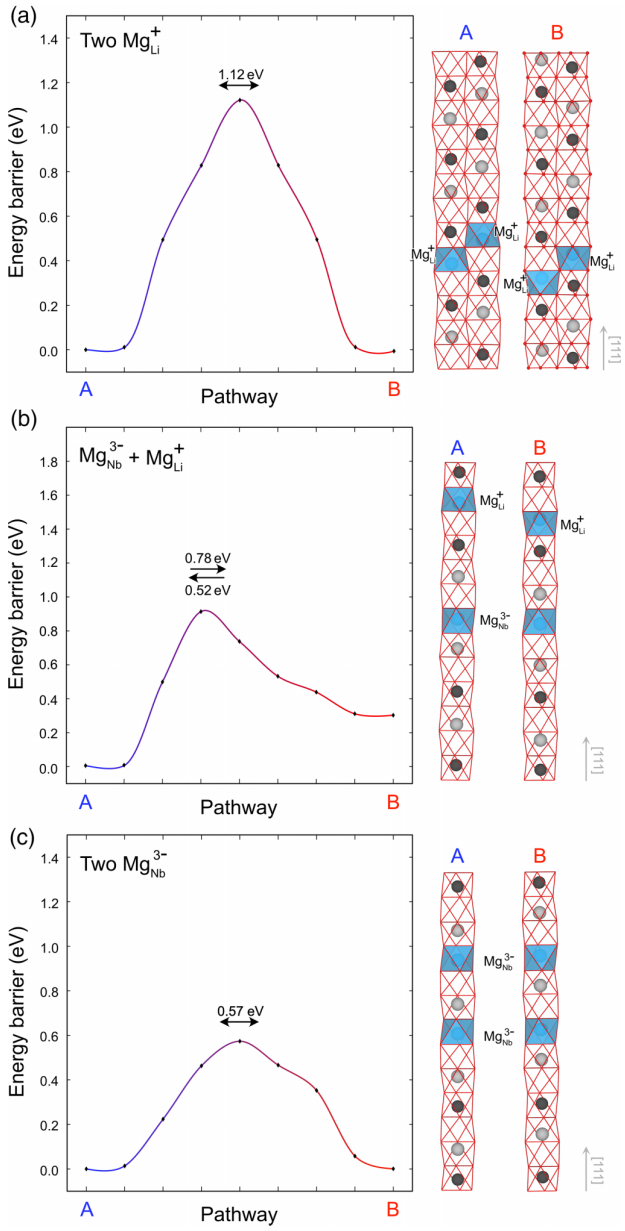


FIG. 8. Activation energies of the poling process for Mg-doped LN with [Mg] = 6.250 mol%. More precisely, the cells containing two $Mg_{Li}^{+}$, one $Mg_{Li}^{+}$ and one single $Mg_{Nb}^{3-}$, and two $Mg_{Nb}^{3-}$ are shown in (a), (b), and (c), respectively.

is influenced by the relative position of the Mg dopants. As a consequence, during poling, where only the Li site (irrespective of their occupation) is affected, the relative position between the $Mg_{Nb}^{3-}$ and $Mg_{Li}^{+}$ would change. This yields a nonsymmetric pathway, where the barrier for the reverse poling (and spontaneous backflip) might not be high enough to guarantee a stable end-structure, also see Fig. 8(b).

In the case of two Mg atoms substituted for each two Li or Nb sites, on the other hand, our calculation again predicts an (almost) symmetric pathway with energy barriers amounting to 1.12 eV and 0.57 eV, respectively.

## IV. SUMMARY AND OUTLOOK

In this study, we investigated the impact of different Mg concentrations on the poling behavior of LN crystals using DFT. For this, we first modeled different defect concentrations and configurations to better understand the distribution of the dopant within the lattice, and computed the defect formation energy. We find that Mg substitutionals on Li sites distribute evenly within the crystal. In addition, they are stable irrespective of the concentration for lower Fermi-level positions, and thus more likely to form for low doping concentrations, whereby a $Mg_{Li}$ could act as a seed point for the domain inversion, since it can be individually moved in the crystal. This may explain the benefit of below coercive field 'wake-up' pulses applied before the actual poling pulse. Mg substitutionals on Nb sites, on the other hand, are only predicted for high doping concentrations, whereas the combination of one Li and one Nb substitutional is most likely for intermediate doping concentrations.

The poling of congruent LN is hampered by the presence of the Nb antisite, yielding either an unsymmetrical reaction pathway, and a high disorder in the Li sublattice, if the $Nb_{Li}$ is not moved, or a rather high energy barrier for the fully inverted configuration. This is in agreement with the defect model presented by Gopalan *et al.* [11]. In addition, we find that if only one type of substitutional is inserted in the supercell, both $Mg_{Li}$ and $Mg_{Nb}$ are helpful in reducing the activation barriers (and therefore also the coercive field strength) required to pol the crystal. Nevertheless, if the distance between two $Mg_{Nb}$ is below about 4 Å, the formation of $Li_{Li}Mg_{Nb}Li_iV_{Li}Nb_{Nb}$ complexes can be observed. Moreover, our calculations for Mg substitutionals located on both Li and Nb sites show that the distance between these substitutionals has a major influence on the ground-state energy of the structure. In fact, configurations which are very favorable in the as-grown crystal turn highly unfavorable after poling. This observation is also reflected by the reaction pathway: In these cases, the pathway is not symmetric anymore, and the activation energy of the backflip is lower compared to the direct transition.

Our results pave the way to a better understanding of the notorious challenges occurring during the poling process of LN crystals heavily doped with Mg. Nevertheless, to fully corroborate the picture, further experimental and theoretical investigations are required. In fact, it is now highly desirable to also understand the role of intermediate configurations, which could occur during the poling process, as well as the influence of Mg dopants on domain walls.

## ACKNOWLEDGMENTS

The DFG (TRR 142/3-2025–Project No. 231447078) is gratefully acknowledged for financial support. We thank the Paderborn Center for Parallel Computing ($PC^2$) and the Höchstleistungsrechenzentrum Stuttgart (HLRS) for grants of high-performance computer time.

## DATA AVAILABILITY

Data will be made available upon reasonable request.

[1] D. Zhu, L. Shao, M. Yu, R. Cheng, B. Desiatov, C. J. Xin, Y. Hu, J. Holzgrafe, S. Ghosh, A. Shams-Ansari, E. Puma, N. Sinclair, C. Reimer, M. Zhang, and M. Lončar, Integrated photonics on thin-film lithium niobate, Adv. Opt. Photon. **13**, 242 (2021).

[2] M. A. Fakhri, H. D. Jabbar, F. H. Alsultany, E. T. Salim, and U. Hashim, Lithium niobate-based sensors: A review, AIP Conf. Proc. **2660**, 020124 (2022).

[3] J. R. Maguire, C. J. McCluskey, K. M. Holsgrove, A. Suna, A. Kumar, R. G. P. McQuaid, and J. M. Gregg, Ferroelectric domain wall p–n junctions, Nano Lett. **23**, 10360 (2023).

[4] A. Suna, O. E. Baxter, J. P. V. McConville, A. Kumar, R. G. P. McQuaid, and J. M. Gregg, Conducting ferroelectric domain walls emulating aspects of neurological behavior, Appl. Phys. Lett. **121**, 222902 (2022).

[5] Y. Jia, L. Wang, and F. Chen, Ion-cut lithium niobate on insulator technology: Recent advances and perspectives, Appl. Phys. Rev. **8**, 011307 (2021).

[6] D. Mandal and S. Banerjee, Surface acoustic wave (SAW) sensors: Physics, materials, and applications, Sensors **22**, 820 (2022).

[7] K. Yang, C. He, J. Fang, X. Cui, H. Sun, Y. Yang, and C. Zuo, Advanced RF filters for wireless communications, Chip **2**, 100058 (2023).

[8] K. Lengyel, Á. Péter, L. Kovács, G. Corradi, L. Pálfalvi, J. Hebling, M. Unferdorben, G. Dravecz, I. Hajdara, Zs. Szaller, and K. Polgár, Growth, defect structure, and THz application of stoichiometric lithium niobate, Appl. Phys. Rev. **2**, 040601 (2015).

[9] T. Volk and M. Wöhlecke, *Lithium Niobate: Defects, Photorefraction and Ferroelectric Switching*, 1st ed., Springer Series in Materials Science (Springer, Berlin, Heidelberg, 2008), Vol. 115.

[10] N. Iyi, K. Kitamura, F. Izumi, J. K. Yamamoto, T. Hayashi, H. Asano, and S. Kimura, Comparative study of defect structures in lithium niobate with different compositions, J. Solid State Chem. **101**, 340 (1992).

[11] V. Gopalan, V. Dierolf, and D. A. Scrymgeour, Defect–domain wall interactions in trigonal ferroelectrics, Annu. Rev. Mater. Res. **37**, 449 (2007).

[12] H. Xu, D. Lee, J. He, S. B. Sinnott, V. Gopalan, V. Dierolf, and S. R. Phillpot, Stability of intrinsic defects and defect clusters in $LiNbO_3$ from density functional theory calculations, Phys. Rev. B **78**, 174103 (2008).

[13] U. Schlarb and K. Betzler, Influence of the defect structure on the refractive indices of undoped and Mg-doped lithium niobate, Phys. Rev. B **50**, 751 (1994).

[14] B. Koppitz, S. Ganschow, M. Rüsing, and L. M. Eng, Ferroelectric hysteresis measurement in the lithium niobate-lithium tantalate single-crystalline family: Prospects for lithium niobate-tantalate, Phys. Status Solidi (a) **222**, 2300967 (2024).

[15] M.-L. Hu, L.-J. Hu, and J.-Y. Chang, Polarization switching of pure and MgO-doped lithium niobate crystals, Jpn. J. Appl. Phys. **42**, 7414 (2003).

[16] Y. Chen, W. Yan, J. Guo, S. Chen, G. Zhang, and Z. Xia, Effect of Mg concentration on the domain reversal of Mg-doped $LiNbO_3$, Appl. Phys. Lett. **87**, 212904 (2005).

[17] H. Xu, D. Lee, S. B. Sinnott, V. Gopalan, V. Dierolf, and S. R. Phillpot, Interactions of defects and domain walls in $LiNbO_3$–insights from simulations, IOP Conf. Ser.: Mater. Sci. Eng. **15**, 012003 (2010).

[18] H. Zhang, Q. Li, H. Zhu, and H. Hu, Optimization of periodic poling of x-cut lithium niobate thin film, Opt. Mater. (Amsterdam) **131**, 112562 (2022).

[19] M. Chen, C. Wang, X.-H. Tian, J. Tang, X. Gu, G. Qian, K. Jia, H.-Y. Liu, Z. Yan, Z. Ye, Z. Yin, S.-N. Zhu, and Z. Xie, Wafer-scale periodic poling of thin-film lithium niobate, Materials **17**, 1720 (2024).

[20] L. Bollmers, T. Babai-Hemati, B. Koppitz, C. Eigner, L. Padberg, M. Rüsing, L. M. Eng, and C. Silberhorn, Surface-near domain engineering in multi-domain x-cut lithium niobate tantalate mixed crystals, Appl. Phys. Lett. **125**, 151101 (2024).

[21] M. Rüsing, J. Zhao, and S. Mookherjea, Second harmonic microscopy of poled x-cut thin film lithium niobate: Understanding the contrast mechanism, J. Appl. Phys. **126**, 114105 (2019).

[22] N. Iyi, K. Kitamura, Y. Yajima, S. Kimura, Y. Furukawa, and M. Sato, Defect structure model of MgO-doped $LiNbO_3$, J. Solid State Chem. **118**, 148 (1995).

[23] F. Abdi, M. Aillerie, P. Bourson, and M. D. Fontana, Defect structure in Mg-doped $LiNbO_3$: Revisited study, J. Appl. Phys. **106**, 033519 (2009).

[24] G. Henkelman, B. P. Uberuaga, and H. Jónsson, A climbing image nudged elastic band method for finding saddle points and minimum energy paths, J. Chem. Phys. **113**, 9901 (2000).

[25] P. Giannozzi, S. Baroni, N. Bonini, M. Calandra, R. Car, C. Cavazzoni, D. Ceresoli, G. L. Chiarotti, M. Cococcioni, I. Dabo, A. D. Corso, S. de Gironcoli, S. Fabris, G. Fratesi, R. Gebauer, U. Gerstmann, C. Gougoussis, A. Kokalj, M. Lazzeri, L. Martin-Samos *et al.*, QUANTUM ESPRESSO: A modular and open-source software project for quantum simulations of materials, J. Phys.: Condens. Matter **21**, 395502 (2009).

[26] P. Giannozzi, O. Andreussi, T. Brumme, O. Bunau, M. B. Nardelli, M. Calandra, R. Car, C. Cavazzoni, D. Ceresoli, M. Cococcioni, N. Colonna, I. Carnimeo, A. D. Corso, S. de Gironcoli, P. Delugas, R. A. DiStasio, Jr., A. Ferretti, A. Floris, G. Fratesi, G. Fugallo *et al.*, Advanced capabilities for materials modelling with QUANTUM ESPRESSO, J. Phys.: Condens. Matter **29**, 465901 (2017).

[27] A. Baldereschi, Mean-value point in the Brillouin zone, Phys. Rev. B **7**, 5212 (1973).

[28] J. P. Perdew, A. Ruzsinszky, G. I. Csonka, O. A. Vydrov, G. E. Scuseria, L. A. Constantin, X. Zhou, and K. Burke, Restoring the density-gradient expansion for exchange in solids and surfaces, Phys. Rev. Lett. **100**, 136406 (2008).

[29] J. P. Perdew, A. Ruzsinszky, G. I. Csonka, O. A. Vydrov, G. E. Scuseria, L. A. Constantin, X. Zhou, and K. Burke, Erratum: Restoring the density-gradient expansion for exchange in solids and surfaces [Phys. Rev. Lett. 100, 136406 (2008)], Phys. Rev. Lett. **102**, 039902(E) (2009).

[30] M. Cococcioni and S. de Gironcoli, Linear response approach to the calculation of the effective interaction parameters in the LDA + U method, Phys. Rev. B **71**, 035105 (2005).

[31] F. Schmidt, A. L. Kozub, T. Biktagirov, C. Eigner, C. Silberhorn, A. Schindlmayr, W. G. Schmidt, and U. Gerstmann, Free and defect-bound (bi)polarons in $LiNbO_3$: Atomic structure and spectroscopic signatures from *ab initio* calculations, Phys. Rev. Res. **2**, 043002 (2020).

[32] F. Schmidt, A. L. Kozub, U. Gerstmann, W. G. Schmidt, and A. Schindlmayr, Electron polarons in lithium niobate: Charge

localization, lattice deformation, and optical response, Crystals **11**, 542 (2021).

[33] F. Schmidt, A. L. Kozub, U. Gerstmann, W. G. Schmidt, and A. Schindlmayr, A density-functional theory study of hole and defect-bound exciton polarons in lithium niobate, Crystals **12**, 1586 (2022).

[34] Y. Li, W. G. Schmidt, and S. Sanna, Intrinsic $LiNbO_3$ point defects from hybrid density functional calculations, Phys. Rev. B **89**, 094111 (2014).

[35] H. Boysen and F. Altorfer, A neutron powder investigation of the high-temperature structure and phase transition in $LiNbO_3$, Acta Crystallogr. Sect. B: Struct. Sci. **50**, 405 (1994).

[36] J. Yang, M. Lai, J. Shang, Q. Li, L. Zhang, and J. Sun, Defect structure of near-stoichiometric Mg-doped $LiNbO_3$ crystals prepared by different method, J. Cryst. Growth **580**, 126478 (2022).

[37] W. Wang, D. Zheng, M. Hu, S. Saeed, H. Liu, Y. Kong, L. Zhang, and J. Xu, Effect of defects on spontaneous polarization in pure and doped $LiNbO_3$: First-principles calculations, Materials **12**, 100 (2019).

[38] C. Freysoldt, B. Grabowski, T. Hickel, J. Neugebauer, G. Kresse, A. Janotti, and C. G. Van de Walle, First-principles calculations for point defects in solids, Rev. Mod. Phys. **86**, 253 (2014).

[39] C. G. Van de Walle and R. M. Martin, Theoretical study of band offsets at semiconductor interfaces, Phys. Rev. B **35**, 8154 (1987).

[40] C. G. Van de Walle and J. Neugebauer, First-principles calculations for defects and impurities: Applications to III-nitrides, J. Appl. Phys. **95**, 3851 (2004).

[41] K. Reuter and M. Scheffler, Composition, structure, and stability of $RuO_2(110)$ as a function of oxygen pressure, Phys. Rev. B **65**, 035406 (2001).

[42] J. C. Slater, Note on Hartree's method, Phys. Rev. **35**, 210 (1930).

[43] J. F. Janak, Proof that $\frac{\partial e}{\partial n_i} = \epsilon$ in density-functional theory, Phys. Rev. B **18**, 7165 (1978).

[44] S. Sanna, T. Frauenheim, and U. Gerstmann, Validity of the Slater-Janak transition-state model within the LDA + $U$ approach, Phys. Rev. B **78**, 085201 (2008).

[45] Y. Li, L. Li, X. Cheng, and X. Zhao, Microscopic properties of Mg in Li and Nb sites of $LiNbO_3$ by first-principle hybrid functional: Formation and related optical properties, J. Phys. Chem. C **121**, 8968 (2017).

[46] T. Kong, Y. Luo, W. Wang, H. Kong, Z. Fan, and H. Liu, Enhanced ultraviolet damage resistance in magnesium doped lithium niobate crystals through zirconium co-doping, Materials **14**, 1017 (2021).

[47] K. Chen, Y. Li, C. Peng, Z. Lu, X. Luo, and D. Xue, Microstructure and defect characteristics of lithium niobate with different Li concentrations, Inorg. Chem. Front. **8**, 4006 (2021).

[48] V. R. Aravind, A. N. Morozovska, S. Bhattacharyya, D. Lee, S. Jesse, I. Grinberg, Y. L. Li, S. Choudhury, P. Wu, K. Seal, A. M. Rappe, S. V. Svechnikov, E. A. Eliseev, S. R. Phillpot, L. Q. Chen, V. Gopalan, and S. V. Kalinin, Correlated polarization switching in the proximity of a 180° domain wall, Phys. Rev. B **82**, 024111 (2010).

[49] T. J. Yang, V. Gopalan, P. J. Swart, and U. Mohideen, Direct observation of pinning and bowing of a single ferroelectric domain wall, Phys. Rev. Lett. **82**, 4106 (1999).

[50] E. A. Eliseev, A. N. Morozovska, G. S. Svechnikov, E. L. Rumyantsev, E. I. Shishkin, V. Y. Shur, and S. V. Kalinin, Screening and retardation effects on 180°-domain wall motion in ferroelectrics: Wall velocity and nonlinear dynamics due to polarization-screening charge interactions, Phys. Rev. B **78**, 245409 (2008).

[51] V. Gopalan, T. E. Mitchell, Y. Furukawa, and K. Kitamura, The role of nonstoichiometry in 180° domain switching of $LiNbO_3$ crystals, Appl. Phys. Lett. **72**, 1981 (1998).

[52] S.-H. Teng, A. Dimou, B. Udofia, M. Ghasemi, M. Stricker, and A. Grünebohm, Control of ferroelectric domain wall dynamics by point defects: Insights from *ab initio* based simulations, J. Appl. Phys. **137**, 154103 (2025).

[53] R. Khachaturyan, Y. Yang, S.-H. Teng, B. Udofia, M. Stricker, and A. Grünebohm, Microscopic insights on field-induced switching and domain wall motion in orthorhombic ferroelectrics, Phys. Rev. Mater. **8**, 024403 (2024).

[54] Z. Fang, Y.-J. Wang, Y.-L. Tang, Y.-L. Zhu, and X.-L. Ma, Huge mobility difference between the neutral and charged steps on 180° domain walls of $PbTiO_3$ by first-principles calculations, J. Appl. Phys. **135**, 044104 (2024).

[55] L. M. Verhoff, M. N. Pionteck, M. Rüsing, H. Fritze, L. M. Eng, and S. Sanna, Two-dimensional electronic conductivity in insulating ferroelectrics: Peculiar properties of domain walls, Phys. Rev. Res. **6**, L042015 (2024).

[56] Z. Xu, X. Zhu, G.-D. Zhao, D. W. Zhang, and S. Yu, Oxygen vacancies stabilized 180° charged domain walls in ferroelectric hafnium oxide, Appl. Phys. Lett. **124**, 012902 (2024).

[57] P. Sen, N. Sisodia, R. K. Choubey, S. Kar, and K. S. Bartwal, Effect of MgO doping on coercive field in $LiNbO_3$ crystals, J. Nonlinear Opt. Phys. Mater. **17**, 175 (2008).

[58] V. Ya. Shur, A. R. Akhmatkhanov, and I. S. Baturin, Micro- and nano-domain engineering in lithium niobate, Appl. Phys. Rev. **2**, 040604 (2015).

[59] M. Younesi, R. Geiss, S. Rajaee, F. Setzpfandt, Y.-H. Chen, and T. Pertsch, Periodic poling with a micrometer-range period in thin-film lithium niobate on insulator, J. Opt. Soc. Am. B **38**, 685 (2021).

[60] L. J. Hu, Y. H. Chang, C. S. Chang, S.-J. Yang, M. L. Hu, and W. S. Tse, Raman and NMR study in MgO-doped $LiNbO_3$ crystal, Mod. Phys. Lett. B **05**, 789 (1991).